

Article

Interaction of Protons with Noble-Gas Atoms: Total and Differential Cross Sections

Musab Al-Ajaleen ^{1,2}  and Károly Tőkési ^{1,3,*} ¹ HUN-REN Institute for Nuclear Research, ATOMKI, 4026 Debrecen, Hungary² Doctoral School of Physics, University of Debrecen, Egyetem tér 1, 4032 Debrecen, Hungary³ HUN-REN Centre for Energy Research, 1121 Budapest, Hungary

* Correspondence: tokesi@atomki.hu

Abstract: We present a classical treatment of the ionization and electron-capture processes in the interaction of protons with neutral noble-gas atoms, namely, Ne, Ar, Kr, and Xe. We used a three-body classical-trajectory Monte Carlo (CTMC) method to calculate the total (TCS) and differential (DCS) cross sections of single-electron processes. The Garvey-type model potential was employed in the CTMC model to describe the collision between the projectile and the target, accounting for the screening effect of the inactive electrons. The TCSs are evaluated for impact energies in the energy range between 0.2 keV and 50 MeV for a number of sub-shells of the targets. The ionization DCS are evaluated for an impact energy of 35 keV, focusing on the outer sub-shells only. We found that our ionization and electron-capture TCSs are in very good agreement with the previous theoretical and experimental data for all targets. Moreover, we presented single (SDCS)- and double (DDCS)-differential cross sections as a function of the energy and ejection angle of the ionized electron for all collision systems.

Keywords: classical trajectory Monte Carlo model; single capture; single ionization; total and differential cross sections; Garvey-type model potential



Citation: Al-Ajaleen, M.; Tőkési, K. Interaction of Protons with Noble-Gas Atoms: Total and Differential Cross Sections. *Atoms* **2024**, *12*, 28. <https://doi.org/10.3390/atoms12050028>

Academic Editor: Kanti M. Aggarwal

Received: 1 February 2024

Revised: 30 April 2024

Accepted: 2 May 2024

Published: 7 May 2024



Copyright: © 2024 by the authors. Licensee MDPI, Basel, Switzerland. This article is an open access article distributed under the terms and conditions of the Creative Commons Attribution (CC BY) license (<https://creativecommons.org/licenses/by/4.0/>).

1. Introduction

The tokamak is regarded the most promising magnetic-confinement design for attaining fusion energy. Nonetheless, certain volatilities can result in plasma disruptions [1,2], which can cause a quick loss of magnetic and thermal energy, commonly referred to as thermal quench. Moreover, when a plasma disruption occurs, the sudden loss of plasma confinement can cause large and destructive forces on the reactor walls and components. Plasma disruption mitigation [3,4] is critical for the safe and reliable operation of plasma-based processes, including fusion reactors. Disruption mitigation aims to prevent or minimize the effects of a plasma disruption in a fusion reactor. Disruption mitigation techniques include injecting substantial quantities of gas into the plasma to rapidly cool and quench it, reducing the amount of energy released during the disruption. Nonetheless, this process leads to an elevation in the quantity of impurities originating from the injected gas within the plasma [5]. Different noble gases and methods [3,4,6–8] have been proposed and examined for their effectiveness in plasma disruption mitigation. Due to differences in mass, reflection coefficients, and ionization, noble-gas particles are anticipated to exhibit distinct behavior at the boundary compared to the majority of plasma constituents [9].

Another purpose of injecting gases into the tokamak is to diagnose the magnetically confined plasma. The injected gases help in measuring the plasma turbulence and density profile of the plasma electron at the edge and in the scrape-off layer [10–15]. Accurate cross sections for induced processes have a critical part in the successful modelling and control of the plasma facing the tokamak reactor wall and components. The present study focuses on single-electron processes, specifically the ionization of targets and electron capture to the projectile, and it is dedicated to providing single, double-differential, and total cross

sections. The interactions under investigation involve protons interacting with neutral inert-gas targets.

The study of ion–atom collisions involving a single electron has been the subject of many theoretical approaches in the scientific community. Classical, quantum, and semi-classical mechanical methods have been developed to compute the cross sections of electron processes in such collisions. Several references for these approaches are reported in [16–18]. Theories used to investigate electron transfer in ion–atom collisions at mid- to high-impact energies include the continuum-distorted-wave method (CDW) [19]. Additionally, other theories such as the classical-trajectory Monte Carlo method (CTMC) [20,21], density functional theory (DFT) [22], two-center atomic-orbitals close-coupling (AO) method [23,24], Oppenheimer–Brinkman–Kramers approximation (OBK) [25–27], and plane-wave first Born approximation (PWFBA) [28] have been employed in this area of research. The advantage of CTMC method is that it is useful when treating atomic collisions where the quantum mechanical ones become intricate, i.e., when higher-order perturbations should be applied, when or many particles take part in the processes [29]. On a microscopic level, plasma is governed by the collisions of its composing particles. For the control of the fusion reactor, we need to know accurately, in principle, all possible reactions and collisional cross sections, like excitation, ionization, recombination, and charge-transfer cross sections. Along this line, in this work, the total cross sections for single-ionization and electron-capture channels in $H^+ - (Ne, Ar, Kr, \text{ and } Xe)$ collision systems are presented in the energy range between 0.2 keV and 50 MeV for a number of sub-shells of the targets. The impact energy is set to 35 keV for differential cross sections. The impact energy is selected to achieve a high interaction probability between the projectile and the plasma. A low impact energy will not allow the projectile to penetrate the plasma, moreover, a large energy will lead to the projectile to pass the plasma with low probability of collision. According to these facts, an impact energy of 35 keV was selected. An advantage of choosing proton as a projectile over heavier particles is that the ejected electrons from the collision are purely from the target. Due to its light mass, protons can ionize targets at lower impact energies compared to heavier particles. The CTMC results are compared with available experimental and theoretical data. The paper is structured into the following three sections: the Theoretical model Section, which provides a review of the classical-trajectory Monte Carlo method in non-Coulombic interactions between interacting particles; the Results and Discussion Section; and the Conclusion Section. Throughout the paper, atomic units are used consistently, unless otherwise specified.

2. Theory

In this work, we used the CTMC method to model ion–atom collisions. The approach involves randomly sampling the initial conditions of colliding particles and subsequently solving the classical equations of motion using numerical methods for a large number of trajectories. The system under consideration is a reduced three-body system consisting of the projectile (H^+), the core of the target (X^+), and one active electron of the target that is initially bound to the target nucleus. Figure 1. shows the schematic diagram of our calculation system.

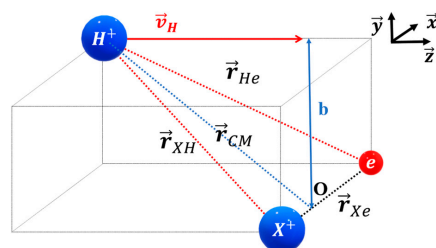


Figure 1. Schematic diagram of the relative position vectors $\vec{r}_{Xe} = \vec{r}_X - \vec{r}_e$, $\vec{r}_{XH} = \vec{r}_X - \vec{r}_H$ and $\vec{r}_{He} = \vec{r}_H - \vec{r}_e$. \vec{r}_{CM} is distance between the projectile and the centre-of-mass (O) of the target system; \vec{v}_H is the projectile velocity and b being the impact parameter.

The interaction between H^+ projectile and the active electron is pure Coulombic. However, we used a Garvey model potential [30,31] to describe the electron–target (X^+) and proton–target (X^+) interaction. This model potential includes an effective charge of the target core, the effective charge depends on the interaction distance between the interacting objects, the form of this model potential is given by the formula:

$$V(r) = q \frac{Z - (N - 1)(1 - Y(r))}{r} \quad (1)$$

where q is a test charge, r is the interaction distance between the electron and target core, Z is number of protons, N is number of electrons in the target, and the function $Y(r)$ is the screening potential, which is given by,

$$Y(r) = \left[(\eta/\zeta) (e^{\zeta r} - 1) + 1 \right]^{-1} \quad (2)$$

The parameters η and ζ were obtained to minimize the energy of an atom or ion with Z larger than 1. The formulae of the parameters η and ζ for the target are given by:

$$\eta = \eta^0 + \eta^1(Z - N) \quad (3a)$$

$$\zeta = \zeta^0 + \zeta^1(Z - N) \quad (3b)$$

where the parameters η^0 , η^1 , ζ^0 and ζ^1 for the targets in our study are given in Table 1, these parameters were calculated by Garvey et al. [30].

Table 1. Parameters values of the targets.

| | ζ^0 | ζ^1 | η^0 | η^1 |
|----|-----------|-----------|----------|----------|
| Ne | 1.792 | 0.4515 | 2.710 | 0.3671 |
| Ar | 0.957 | 0.2165 | 3.500 | 0.2560 |
| Kr | 1.351 | 0.1872 | 4.418 | 0.1611 |
| Xe | 1.044 | 0.1107 | 5.101 | 0.1316 |

In Figure 2, we present the effective-charge profile of various targets as a function of the interaction distance with the active electron. The effective charge of all objects decays exponentially with increasing interaction distance. Moreover, the effective-charge values become almost equal for interaction distances larger than 3 *a.u.*, and they approach to unity.

The total potential energy V for the current three-body system can then be written as:

$$V = \frac{q_e Q(s)}{s} + \frac{q_p Q(x)}{x} + \frac{q_e q_p}{d} \quad (4)$$

where s (\vec{r}_{Xe}), x (\vec{r}_{XH}) and d (\vec{r}_{He}) are the separation between the interaction particles, q_e and q_p are electron and proton charges, respectively. $Q(s)$ and $Q(x)$ represent the effective charge [$Q(r) = Z - (N - 1)(1 - Y(r))$] of the target corresponding to the electron and to the proton, respectively.

The equations of motion for the system were generated using the Hamiltonian. To solve the equations for a large number of projectiles numerically, the adaptive Runge–Kutta method was employed.

The position of H^+ is determined by its initial distance from the centre of mass of the target system, denoted as $r_{CM,0}$, as well as the impact parameter b (see Figure 1). We note that the maximum values of b (b_{max}) were selected in such a way that the ionization and electron-capture processes are negligible above the values of b_{max} . The value of $r_{CM,0}$ is chosen such that the H^+ -electron interaction is much smaller than the X^+ -electron interaction. In terms of the projectile ion's initial momentum vector, which is assumed to be in the z direction at the start, it is determined by the impact velocity v_H of the

projectile ion in relation to the target’s center of mass. The procedure initially introduced by Reinhold and Falcón [32] is utilized to determine the initial position and momentum vector of the active target electron, which is initially bound to the target nucleus and moves in a non- Coulombic potential. The process of selecting the initial conditions depends on constraints related to the binding energy of the electron in a specific shell. The coordinate of the electron is confined to a specific interval dictated by $E_o - V(s) > 0$, where E_o is the ionization energy of the electron and $V(s)$ is the model potential of the electron and the target core. Transforming position and momentum variables of the electron into uniformly distributed ones involves consecutive coordinate changes. The first transformation involves defining parameters, followed by introducing initial distributions and performing a second transformation to obtain the desired distribution. Random selection within the defined intervals produces the initial conditions for the active electrons.

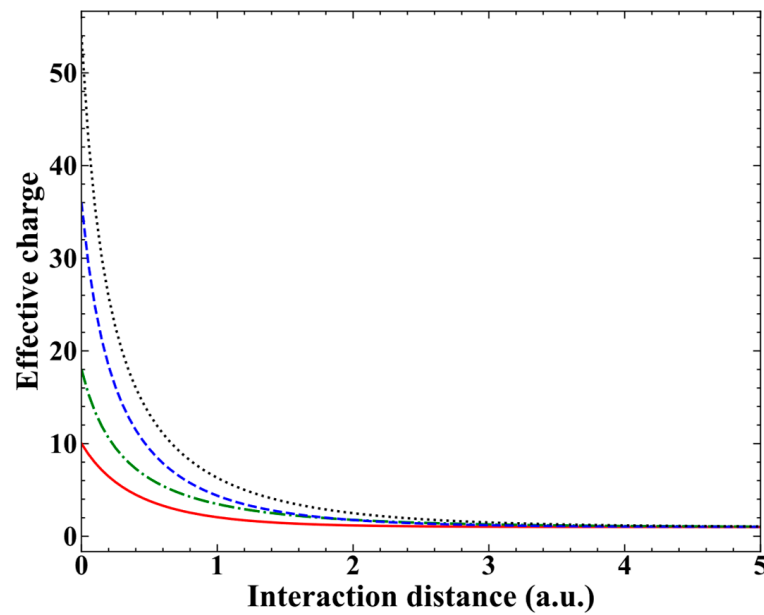


Figure 2. The distance-dependent effective charge as a function of interaction distance between the active electron of the target core and different targets cores. Red solid line, Ne; green dotted-dashed line, Ar; blue dashed line, Kr; black dotted line, Xe.

The total, single-, and double-differential cross sections are evaluated using the following formulae,

$$\sigma = \frac{2\pi b_{max}}{N_{tot}} \sum_{i=1}^{N_t} b_i \tag{5}$$

$$\frac{d\sigma}{dE} = \frac{2\pi b_{max}}{N_{tot}\Delta E} \sum_{i=1}^{N_t} b_i \tag{6}$$

$$\frac{d\sigma}{d\Omega} = \frac{2\pi b_{max}}{N_{tot}\Delta\Omega} \sum_{i=1}^{N_t} b_i \tag{7}$$

$$\frac{d^2\sigma}{d\Omega dE} = \frac{2\pi b_{max}}{N_{tot}\Delta\Omega\Delta E} \sum_{i=1}^{N_t} b_i, \tag{8}$$

where N_{tot} is the total number of trajectories calculated for impact parameters less than b_{max} , and N_t is the number of trajectories that satisfy the criteria for the given atomic process, and b_i is the actual impact parameter for the trajectory corresponding to the atomic process

under consideration in the energy interval ΔE and the emission-angle interval $\Delta\Omega$ of the electron. The statistical error for a given measurement has the form

$$\Delta\sigma = \sigma \left(\frac{N_{tot} - N_t}{N_{tot}N_t} \right)^{1/2}. \quad (9)$$

3. Results and Discussion

In this section we present the results of total cross section for both ionization and electron-capture processes, as well as the single- and double-differential cross section for ionization process. The classical-trajectory Monte Carlo (CTMC) method is employed to solve the scattering problem. Table 2 shows the binding energies of the targets for the shells used in our study.

Table 2. Binding energies (eV) used in our simulations.

| | Ne | Ar | Kr | Xe |
|----|------|-------|------|-------|
| 2s | 48.5 | | | |
| 2p | 21.6 | 248.4 | | |
| 3s | | 29.3 | | |
| 3p | | 15.7 | | |
| 3d | | | 93.8 | 676.4 |
| 4s | | | 27.5 | 213.2 |
| 4p | | | 14.1 | 145.5 |
| 4d | | | | 67.5 |
| 5s | | | | 23.3 |
| 5p | | | | 12.1 |

The total cross section of electron-capture and ionization, and the differential cross section, are presented for the collision of proton (H^+) with Ne, Ar, Kr, and Xe. For the DCS, the impact energy of proton was set to 35 keV for fusion-plasma diagnostic applications, while we used a wider energy range for TCS to cover more research areas. The grayed cells represent unused sub-shells in the study.

There are three points we want to draw attention to regarding our methodology, which are: the energy range of the CTMC, the nucleus–nucleus interaction, and the inner-shells contribution. The CTMC method is a reasonable approximation for medium to high impact energies, but it lacks accuracy at low energies, i.e., slow projectiles. The contribution of nucleus–nucleus interaction to the collision cross sections is negligible [19], as we verified in our previous works [33,34], performing calculations with and without the nuclear potential.

Figure 3 shows the TCS of the single-electron ionization from Xe by protons for various sub-shells. For impact energies below 50 keV, we clearly see that the contribution of the inner shells to the TCS is insignificant, with the ionization from the 5p shell approximately approaching the TCS. Beyond 50 keV, the contribution of inner shells to the TCS increases when increasing the impact energy. According to this result, we will include the contributions of the inner shells into the TCS cross sections. However, for the case of ionization differential cross section at impact energy of 35 keV, it is a good approximation to consider only the 5p shell, see green shaded area in Figure 3. From Figure 3, we can also see that the cross section maxima of inner shells shift to higher energies. Moreover, the TCS of the 5s shell surpasses the TCS of the 4d shell up to impact energies around 120 keV, but above this energy, the TCS of the 4d shell becomes larger.

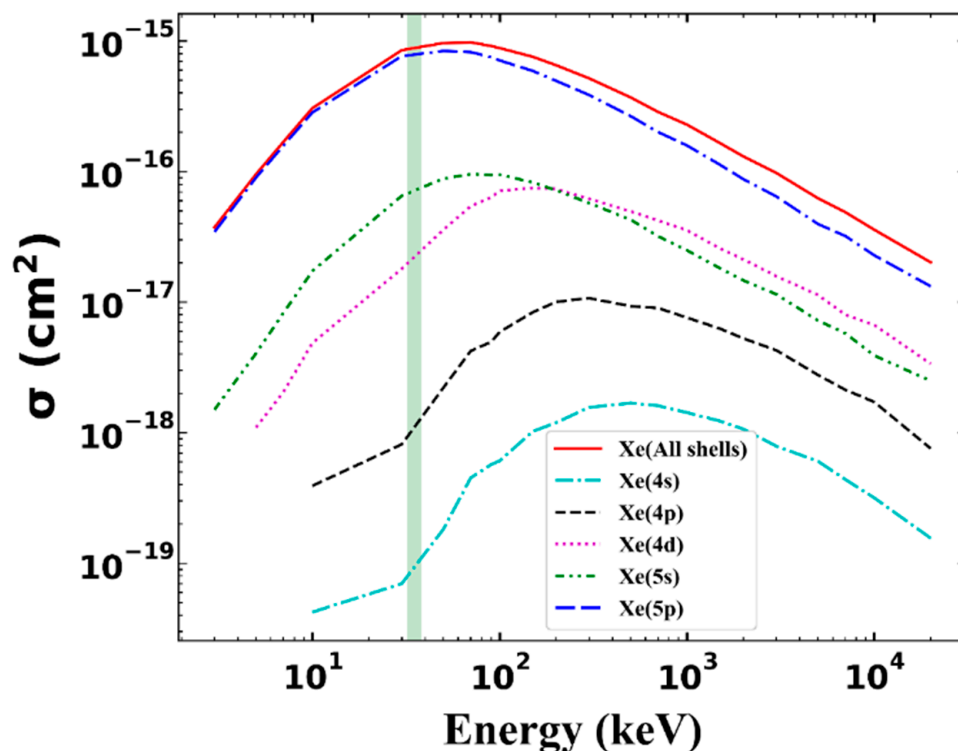


Figure 3. Total cross section of ionization channel of the collision $H^+ - Xe$ for 3d, 4s, 4p, 4d, 5s and 5p shells. Our theoretical CTMC results: cyan dashed-dotted line, 4s; black dashed line, 4p; magenta dotted line, 4d; green dashed-dotted-dotted line, 5s; blue dashed-dashed-dotted line, 5p. Red solid line is the sum of the sub-shells of Xe. The green shaded area represents the total cross section at impact energy near 35 keV.

3.1. Total Cross Section for Single-Electron Capture

Figure 4 shows the total cross sections of electron capture for the interaction of proton with noble gases. The impact-energy range of TCS for the electron-capture channel investigated is 0.2–1300 keV. The TCS curves have a parabola-like shape, with TCS having the peak at impact energies around 10 keV, 4 keV, 1 keV and 0.5 keV for Ne, Ar, Kr and Xe, respectively.

In comparing the maximum TCS for the four elements, Ne has the lowest TCS, Xe has the highest, and Ar and Kr have approximately the similar values. But we note that the TCS of Kr is slightly higher. These results are attributed partly to the binding energy of the outermost shell, i.e., Ne has the highest, Xe the lowest, and Ar and Kr have close binding energies of the outermost shell (see Table 2), and partly because the outermost shell contributes the most to the overall TCS (see Figure 3).

In the case of $H^+ - Ne$ collision (see Figure 4a), the experimental data by Allison [35], Williams et al. [36], and Rudd et al. [37] are in an energy range below 200 keV, and are in a very good agreement with each other. Moreover, the experimental data by Varghese et al. [38] and Almeida et al. [39] are in very good agreement with each other as well, but for impact energies higher than 300 keV. Regarding to the theoretical references, the data by Nikolaev [25], Belkic [19], and Houmar et al. [28] are in agreement with each other and with the experimental data beyond impact energy of 300 keV. However, below this energy, the data of Belkic [19] and Houmar et al. [28] lose agreement, while the data of Nikolaev [25] still kept the agreement with the experimental data. In his study, Nikolaev [25] used the Brinkman–Kramers approximation. Our data follow the trend of the experimental data, but slightly overestimate it.

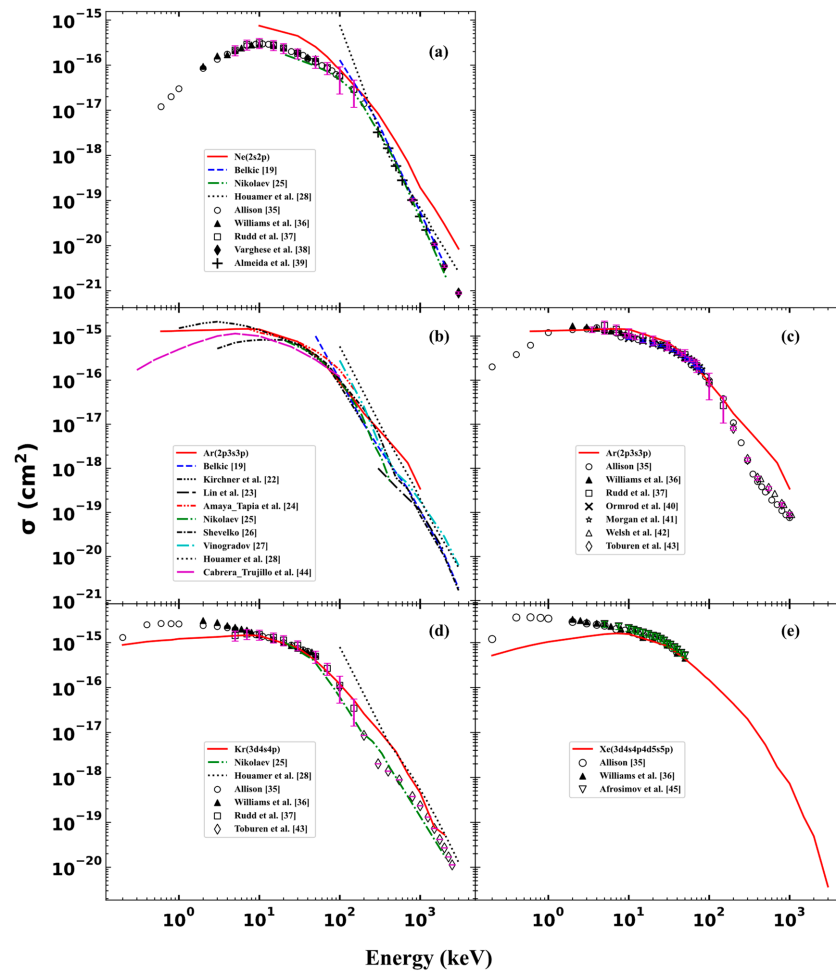


Figure 4. Total cross section of electron-capture channel of the collision (a) $H^+ - Ne$ for 2s and 2p shells, (b) $H^+ - Ar$ for 2p, 3s, and 3p shells, theoretical references, (c) $H^+ - Ar$ for 2p, 3s, and 3p shells, experimental references, (d) $H^+ - Kr$ for 3d, 4s, and 4p shells, and (e) $H^+ - Xe$ for 3d, 4s, 4p, 4d, 5s and 5p shells. Red solid line: Our theoretical CTMC results. Experimental results are plotted using scatter markers; theoretical results are plotted with lines.

For the case of the $H^+ - Ar$ collisions, we present the theoretical and the experimental data in Figures 4b and 4c, respectively. We can clearly see that the experimental references exhibit very good agreement. Moreover, below 2 keV, only experimental data are available by Allison [35]. Our results agree well with the experimental results by Allison [35], Williams et al. [36], Ormrod et al. [40], Morgan et al. [41], and Rudd et al. [37] in the energy range between 0.4 keV and 200 keV; beyond this energy, our results slightly overestimate the experimental results by Allison [35], Welsh et al. [42], and Toburen et al. [43]. This is also true for most of the theoretical results in Figure 4b. Regarding the theoretical references, the data of Houmar et al. [28] slightly overestimate the experimental data, while Belkic [19] and Vinogradov et al. [27] agree well with the experimental and other theoretical data. It is worth noting that Houmar et al. [28] and Vinogradov et al. [27] do not have data below 100 keV, while Belkic [19] does not have data below 50 keV. Nikolaev [25] and Shevelko [26] also show very good agreement with each other. For impact energy below 20 keV, the theoretical data differ from each other. Although Kirchner et al. [22] and Cabrera Trujillo et al. [44] show a slight disagreement with each other, they both follow the trend of experimental results of Allison [35]. Kirchner et al. [22] used density functional theory (DFT) to build the time-dependent independent particle model (IPM) in the energy range between 1 keV and 200 keV. Cabrera Trujillo et al. [44] employed

semiclassical coupled-channel and a nonadiabatic electron-nuclear dynamics approach in the energy range between 0.01 keV and 100 keV.

For the collision of H^+ with Kr (Figure 4d), the only available theoretical data are provided by Nikolaev [25] and Houmar et al. [28]. Regarding the experimental data, for impact energy below 20 keV, we only have data from Allison [35]. For impact energy above 200 keV, we have the data by Toburen et al. [43]. Similar to the previously discussed collision systems, the Houmar et al. [28] result overestimate the experimental data, while data by Nikolaev [25] show very good agreement with the experimental data. Our calculated cross sections also show very good agreement with the experimental data in the energy range between 5 keV and 200 keV. Below 5 keV, our results underestimate the data of Allison [35] and Williams et al. [36]. Above 200 keV, our results slightly overestimate the data of Toburen et al. [43] and Nikolaev [25]. It is interesting to note that we can also see a bit (the most prominent here among the investigated targets) a shoulder-like structure in the energy range around 300 keV impact energy. The detailed investigations of this structure we plan to show in our forthcoming publication.

For the case of H^+ – Xe collisions (in Figure 4e) there are no theoretical references, and the available experimental data are limited to the energy range between 0.2 keV and 50 keV. These data are by Allison [35], Williams et al. [36], and Afrosimov et al. [45]. Our data are in very good agreement with the existing experimental results at energy between 5 keV and 50 keV. However, below 5 keV, our data underestimates the results of Allison [35]. According to our results from the collisions of H^+ – Ne, H^+ – Ar, and H^+ – Kr, we have confidence in the accuracy of our results of H^+ – Xe system for impact energy above 50 keV.

3.2. Total Cross Section for Single Ionization

Figure 5 shows the total cross sections of ionization for the interaction of proton with noble gases. The investigated impact-energy range of TCS for the ionization channel was between 1 keV and 50 MeV. The TCS have the maximum at impact energies, around the range of 60–70 keV for all targets.

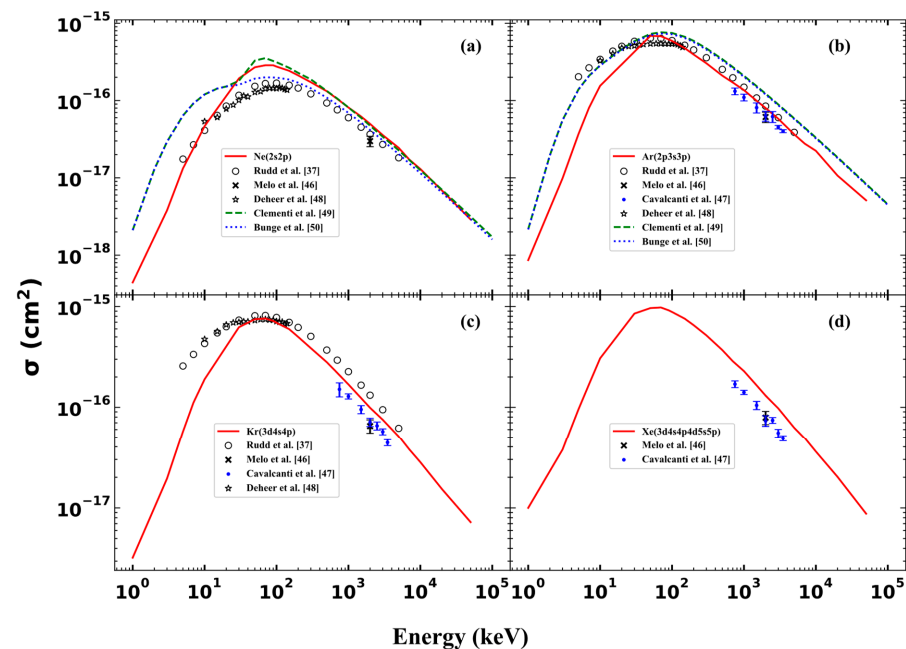


Figure 5. Total cross section of ionization channel in the collision (a) H^+ – Ne for 2s and 2p shells, (b) H^+ – Ar for 2p, 3s, and 3p shells, (c) H^+ – Kr for 3d, 4s and 4p shells, and (d) H^+ – Xe for 3d, 4s, 4p, 4d, 5s, and 5p shells. Our theoretical CTMC results. Experimental results are plotted using scatter markers; theoretical results are plotted with lines.

Comparing the peaks of the ionization TCS for the four elements, we arrive at the same conclusion as for the case of the electron capture, i.e., Ne has the lowest, Xe has the highest; Ar and Kr have approximately the same values, and the value of Kr is slightly higher. These results are attributed to the binding energy of the outermost shell of the targets, as discussed for the case of the single-electron capture.

For a single ionization in the collision of a proton with Ne, Ar, and Kr, Rudd et al. [37] performed experiments in the impact-energy range between 5 and 5000 keV. Melo et al. [46] studied the ionization of Ne, Ar, Kr, and Xe at 2 MeV protons. Cavalcanti et al. [47] studied multiple ionization of Ar, Kr, and Xe in the energy between 0.75 and 3.50 MeV. De Heer et al. [48] presented an ionization cross section of proton collision with Ne, Ar, and Kr in the range 10–140 keV. The results by De Heer et al. [48] are in agreement with the results by Rudd et al. [37]. Regarding the theoretical data, Clementi et al. [49] and Bunge et al. [50] provided data for all sub-shells of $H^+ - Ne$ and $H^+ - Ar$ collisions. However, for $H^+ - Kr$ and $H^+ - Xe$ collisions, Clementi et al. [49], Bunge et al. [50] and others [51–54] provided ionization TCS for inner-shells only, namely, K and L shells. for $H^+ - Kr$ collision, and K, L, and M shells for $H^+ - Xe$ collision. We did not show these results in our present work due to their negligible contribution to the overall TCS, as discussed in Figure 3. Clementi et al. [49] and Bunge et al. [50] employed Roothaan–Hartree–Fock (RHF) method in their study.

In Figure 5a, we present TCS results for single-electron ionization of Ne by proton impact. Below 25 keV, our results are in very good agreement with Rudd et al. [37], while results by Clementi et al. [49] and Bunge et al. [50] are equal but overestimate the experimental data. Above 25 keV, the results of Bunge et al. [50] diverge from the data of Clementi et al. [49] and showed a very good agreement with experimental data. In 25–400 keV range, both our results and those of Clementi et al. [49] overestimate the experimental data by Rudd et al. [37] and De Heer et al. [48]. Beyond 400 keV, our results show relatively good agreement with theoretical and experimental data by Rudd et al. [37] and Melo et al. [46].

For the results of the interaction of protons with Ar (see the Figure 5b), Clementi et al. [49], and Bunge et al. [50] fully overlap; furthermore, they overestimate the experimental data of Rudd et al. [37] and De Heer et al. [48] for impact energy above 50 keV. At the same time, however, they show good agreement with the experimental data below this energy. Conversely, our results show very good agreement with experimental data above this energy but underestimate it below 50 keV.

In the collision of $H^+ - Kr$ (see Figure 5c), our results follow the trend of the experimental data of Rudd et al. [37]. Beyond 30 keV, our data are in good agreement with the experimental data, but below this energy, our results underestimate the experimental data by Rudd et al. [37] and De Heer et al. [48].

For the case of $H^+ - Xe$ collision (see Figure 5d), the available experimental data to compare with are by Melo et al. [46] and Cavalcanti et al. [47]. Our ionization cross sections slightly overestimate the cross sections by Melo et al. [46] and Cavalcanti et al. [47].

3.3. Single-Differential Cross Sections (SDCS) of Ionization

Figures 6 and 7 show the energy and angular single-differential cross sections (SDCS) for an impact energy of 35 keV. During the calculations, only the outer shells were considered, except for Xe, where 5d and 5p shells were considered. In Figure 6, the energy distribution of SDCS curves for different targets follows a similar trend but has different magnitude in cross sections. This can be attributed to the fixed charge of +1 for the projectile throughout the interaction with the target. Xe(4d) has the lowest SDCS cross sections, which is a result of its high binding energy. On the other hand, Xe(5p) has the highest SDCS cross sections due to its low binding energy, and its cross-section trend is similar to those of Ar(3p) and Kr(4p). Additionally, the SDCS values of Ar(3p) and Kr(4p) are nearly identical, which can be attributed to the minimal difference in their binding energies. Furthermore, the SDCS for all targets maintains almost a constant value for ejection energy

less than 20 eV; above this energy, the cross-section decreases drastically. Moreover, due to the fact that, compared to the low energy collision, relatively high-energy electrons are obtained ($E > 100$ eV), the signature of multiple scattering in the electron spectra can be seen. The binary peaks are clearly visible, but at higher electron energies, the signature of higher order collision sequences, the so-called Fermi-shuttle-type ionization [55], can also be recognized. The detailed investigation of the multiple-scattering sequence will be published in our forthcoming publication.

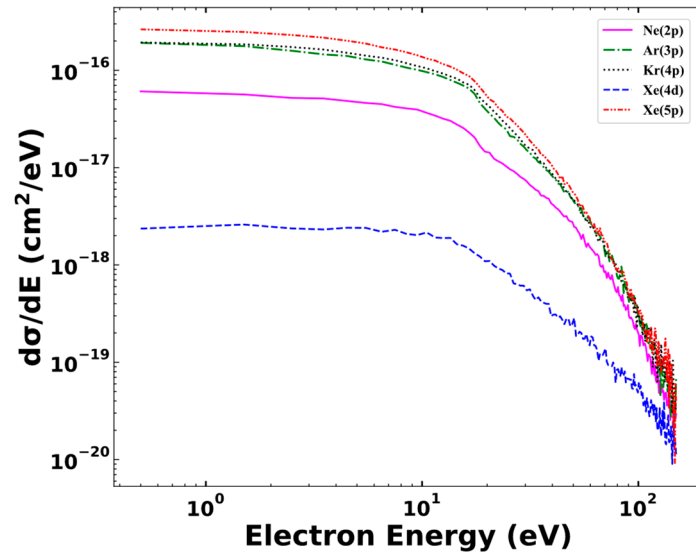


Figure 6. Energy distribution of the electrons emitted from the collision of 35 keV protons (H^+). Magenta solid line, $Ne(2p)$; green dashed-dotted line, $Ar(3p)$; black dotted line, $Kr(4p)$; blue dashed line, $Xe(4d)$; red dashed-two-dots line, $Xe(5d)$.

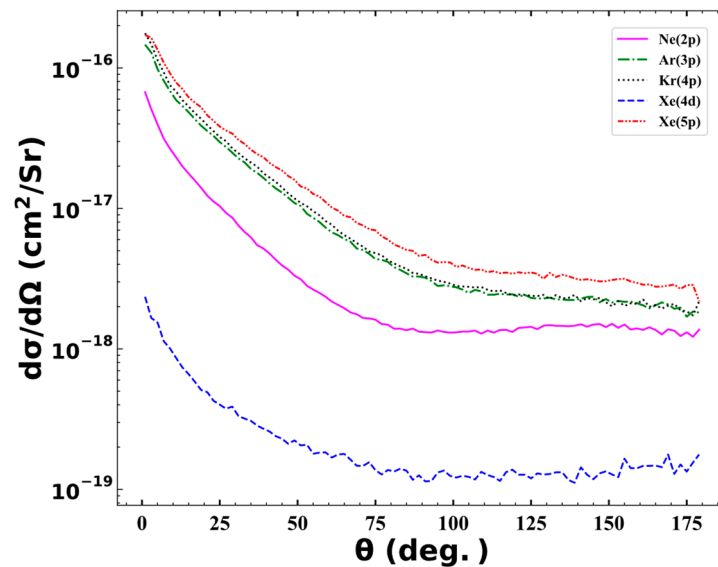


Figure 7. Angular distribution of the electrons emitted from the collision of 35 keV protons (H^+). Magenta solid line, $Ne(2p)$; green dashed-dotted line, $Ar(3p)$; black dotted line, $Kr(4p)$; blue dashed line, $Xe(4d)$; red dashed-two-dots line, $Xe(5d)$.

The results presented in Figure 7 provide insight on the angular distribution of SDCS curves of the studied targets. It is observed that the angular distribution of SDCS curves of $Ar(3p)$, $Kr(4p)$, and $Xe(5p)$ follows a similar pattern, starting with high SDCS values at small angles, which then decrease rapidly until the ejection angle is around 90 degrees,

followed by a gradual decrease in the SDCS. On the other hand, the angular distribution of SDCS curves of Ne(2p) and Xe(4d) follows almost the same pattern, with SDCS values starting with high values at small angles, then rapidly decreasing until the ejection angle is around 90 degrees, and then maintaining constant SDCS values. Furthermore, the angular distribution of SDCS curves of Ne(2p) and Xe(4d) are lower than that of their counterparts Ar(3p), Kr(4p), and Xe(5p). This can be attributed to the larger binding energies of Ne(2p) and Xe(4d).

3.4. Double-Differential Cross Sections (DDCS)

In DDCS calculations, only the outer shell is considered. Figure 8 shows the DDCS contour as a function of the energy and ejection angle of the ejected electrons in collision between 35 keV protons with the neutral noble gases (Ne(2p), Ar(3p), Kr(4p) and Xe(5p)). The majority of the ionized electrons are ejected in forward scattering at angles less than 80 degrees and energies less than 20 eV. Notably, for electrons ejected with energy larger than 100 eV, the DDCS is very small. Figures 9 and 10 provide more detail about the energy distribution of DDCS at selected angles, while Figure 11 shows the angular distribution of the DDCS at selected energy ranges.

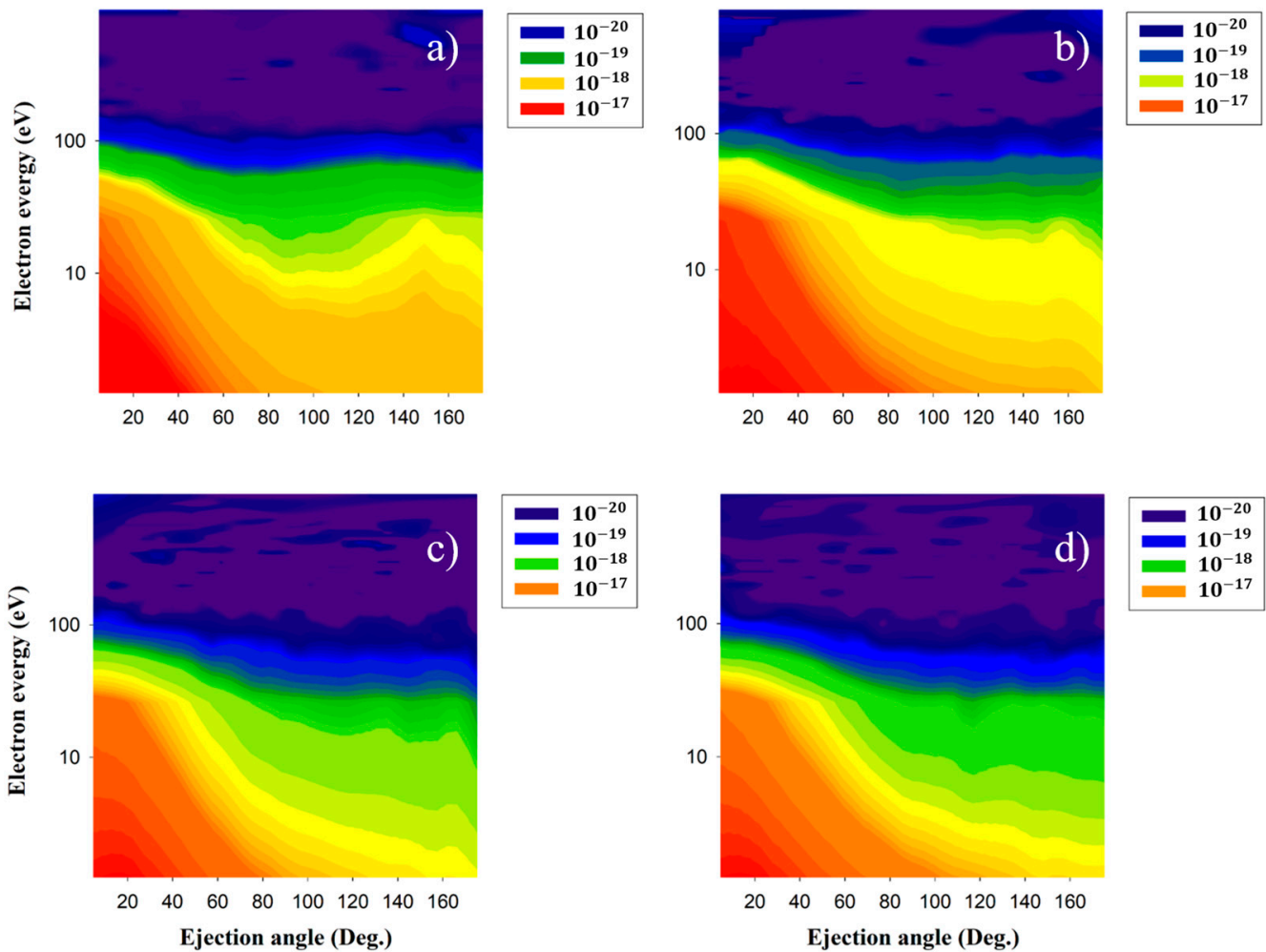


Figure 8. Double-differential cross section (DDCS) (in $\text{cm}^2/\text{eV.Sr}$) of ionization channel as a function of ejection angle and electron energy in the collision of 35 keV protons (H^+) with, (a) Ne(2p), (b) Ar(3p), (c) Kr(4p), (d) Xe(5p).

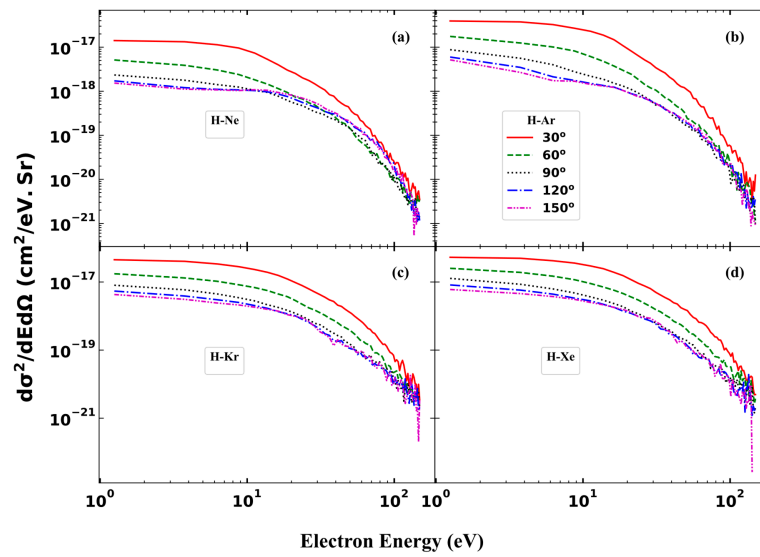


Figure 9. Double-differential cross section (DDCS) of ionization channel as function of an electron energy in the collision of 35 keV protons (H^+) with, (a) Ne(2p), (b) Ar(3p), (c) Kr(4p), and (d) Xe(5p). The ejection angles: red solid line, 30°; green dashed line, 60°; black dotted line, 90°; blue dashed-dotted line, 120°; and magenta dashed-two-dots line, 150°.

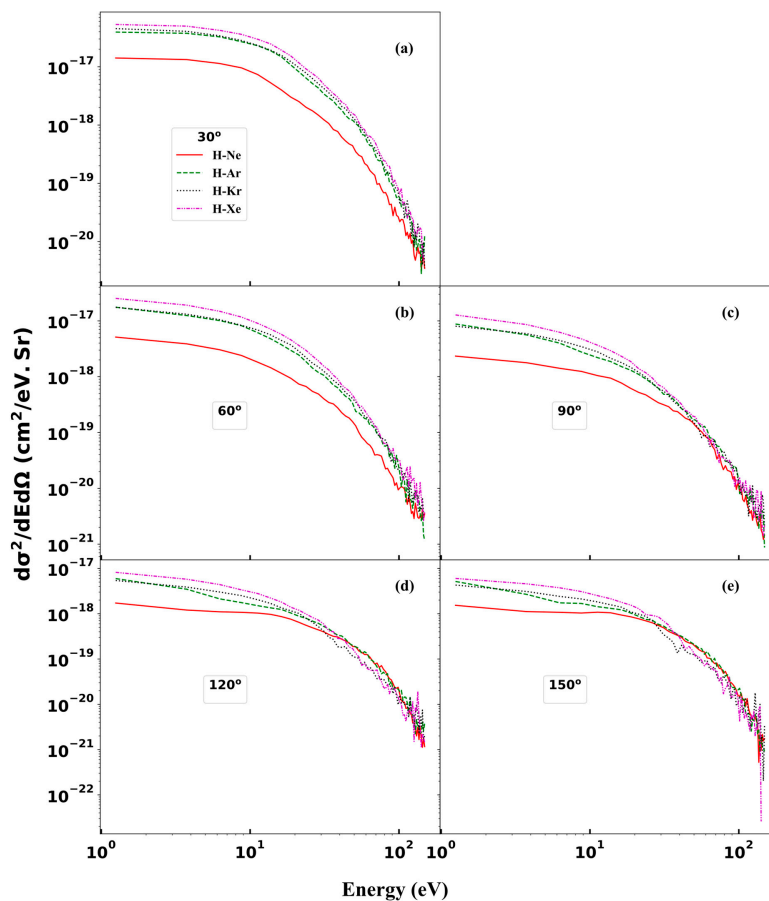


Figure 10. Double-differential cross section (DDCS) of ionization channel as function of electron energy in the collision of 35 keV protons (H^+) at ejection angles, (a) 30°, (b) 60°, (c) 90°, (d) 120°, and (e) 150°. The targets: red solid line, Ne(2p); green dashed line, Ar(3p); black dotted line, Kr(4p); and magenta dashed-two-dots line, Xe(5p).

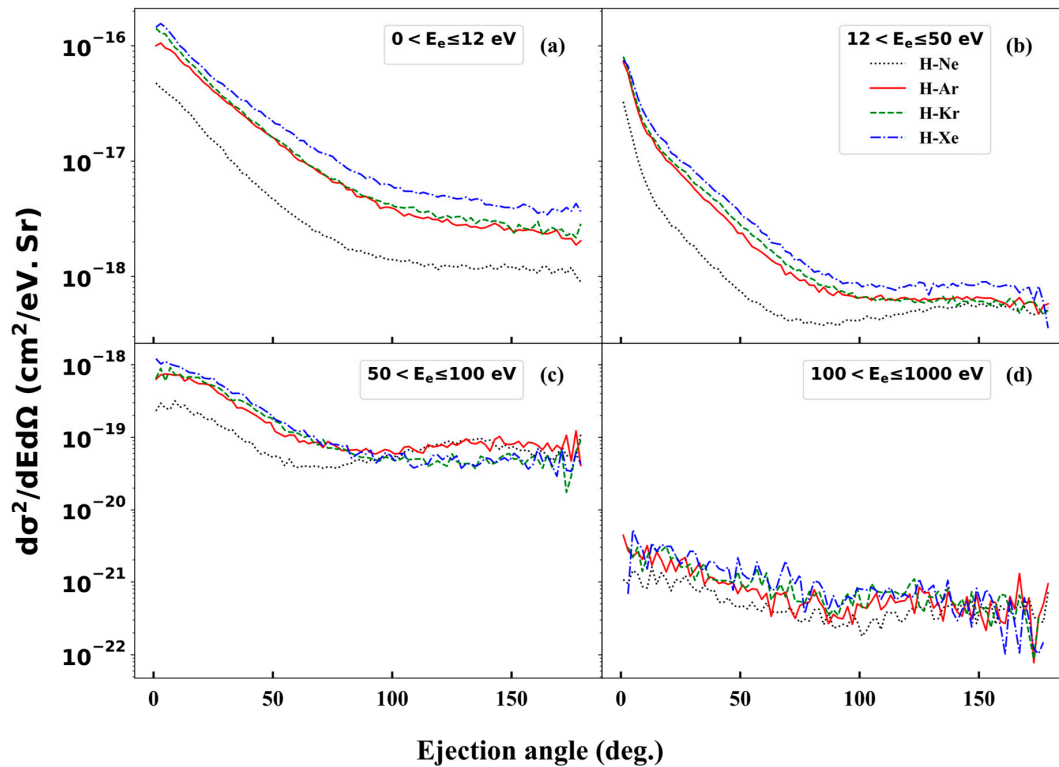


Figure 11. Double-differential cross section (DDCS) of ionization channel as function of ejection angle in the collision of 35 keV protons (H^+) with, (a) $0 < E_e \leq 12$ eV, (b) $12 < E_e \leq 50$ eV, (c) $50 < E_e \leq 100$ eV, and (d) $100 < E_e \leq 1000$ eV. The targets: black dotted line, Ne(2p); red solid line, Ar(3p); green dashed line, Kr(4p); and blue dashed-dotted line, Xe(5p).

In Figure 9, the DDCS is plotted as a function of electron energy at selected angles for various targets. The angles in Figures 9 and 10 are taken in the range between 0° and 10° . The DDCS is largest at forward scattering, especially at ejection angle of 30° for all targets. The DDCS at ejection angles of 120° and 150° are almost identical. For targets Ar(3p), Kr(4p), and Xe(5p), the DDCS at 120° and 150° angles are the smallest across the entire energy range. However, this is not entirely true for the case of Ne(2p); the DDCS for Ne(2p) is smallest at these angles for electron energy below 20 eV. Beyond this energy, the DDCS at 120° and 150° becomes larger than that for ejection angles of 60° and 90° .

In Figure 10, the DDCS is plotted as a function of electron energy for various targets at selected angles. At 30° (see Figure 10a), the DDCS for Ne(2p) is the smallest among all targets for all energies. For Ar(3p) and Kr(4p), the DDCSs are almost equal, with the DDCS of Kr(4p) slightly higher due to the close binding energies of outer shells. Xe(5p) has the highest DDCS, but the difference is not significant compared to both Ar(3p) and Kr(4p). For all targets, the DDCS remains nearly constant below around 10 eV. Above this energy, the DDCS decreases drastically. At ejection angle 60° (see Figure 10b), the DDCS behavior is similar to that at 30° ; however, a slight difference is that the DDCS does not remain constant at low energies but starts decreasing from the beginning.

At right-angle scattering (90° , see Figure 10c), the DDCSs of Ar(3p), Kr(4p), and Xe(5p) show similar behavior compared to the DDCSs at ejection angle 60° for energies less than around 40 eV. Additionally, the DDCS of Ne(2p) at 90° is less steep compared to the DDCS at ejection angle 60° .

In backward scattering at ejection angles of 120° and 150° (see Figure 10d,e), the DDCSs exhibit the same behavior. The DDCS of Ne(2p) maintains a constant value for energy below around 20 eV. Furthermore, the DDCSs of Ne(2p) and Ar(3p) for energies below around 40 eV are lower than the DDCSs of Kr(4p) and Xe(5p). However, for energies

between around 40 eV and 100 eV, the DDCSs of Ne(2p) and Ar(3p) are higher than those of Kr(4p) and Xe(5p).

In Figure 11, the DDCS is plotted as a function of ejection angles for various targets and at selected electron energy ranges. In Figure 11a, we present the DDCS for electrons with energies less than 12 eV. Xe(5p) exhibits the largest DDCS across all angles, while Ne(2p) exhibits the lowest. The DDCSs of Ar(3p) and Kr(4p) have close magnitudes. All curves at this energy range start high at small angles, then they decrease drastically until reaching a right-angle scattering. For the backward scattering, the DDCS curves become less steep and decrease gradually.

For electron energies ranging between 12 eV and 50 eV (see Figure 11b), the DDCS curves of Ar(3p), Kr(4p) and Xe(5p) show similar behavior. In this electron energy range, the DDCS curves drastically decrease with increasing the ejection angles in the forward scattering, compared to the DDCS curves of electrons with energies less than 12 eV (see Figure 11a). For the backward scattering of Ar(3p), Kr(4p), and Xe(5p), the DDCS values become almost constant. In the case of Ne(2p), the DDCS curve also shows a drastic decrease in the forward scattering, reaching minimum value at right-angle scattering. In the backward scattering, the DDCS curve starts to show a small increase when the ejection angle increases.

For electron energies ranging between 50 eV and 100 eV (see Figure 11c), the DDCS values are smaller compared to previous electron energy ranges. The DDCS curves of Kr(4p) and Xe(5p) are almost equal and decrease slowly until they reach the 90° scattering, then they show almost constant values. The DDCS values of Ar(3p) are nearly equal to the DDCS values of Kr(4p) and Xe(5p) in the forward scattering. However, the DDCS curve has a minimum at 90° scattering. The DDCS values increase in the backward scattering. The DDCS values of Ne(2p) are much smaller than those of Ar(3p), Kr(4p), and Xe(5p) in forward scattering. The DDCS curve of Ne(2p) shows a minimum around the 90° scattering similarly to the case of Ar(3p). Moreover, in the backward scattering, the DDCS values of Ne(2p) increase slowly, and they are almost equal to the DDCS values of Ar(3p).

For electron energies ranging between 100 eV and 1000 eV (see Figure 11d), the DDCS values are very small compared to the lower-energy cases discussed earlier. Due to the low calculation statistic effected by a low number of ionized electrons, the DDCS curves for all targets are now tangled, especially for ejection angles larger than 120°, and they show very close values to one another. However, the DDCS values of Ne(2p) are the smallest by a narrow margin, while the DDCS values of Xe(5p) are the largest by a similarly small margin for ejection angles less than 120°.

4. Conclusions

We have presented the total (TCS) and differential (DCS) cross sections of the interaction of protons H^+ with neutral noble gases. We used the three-body CTMC calculations based on Garvey-type model potential. In the model potential, only one active electron was included in the interaction dynamics, while the remaining electrons contributed to the screening effect. The TCSs of single-electron capture and single-electron ionization from different sub-shells were presented and discussed for the 0.2 keV–50 MeV energy range. The ionization DCSs were presented and discussed for impact energy of 35 keV, focusing only on the outer sub-shells of the targets. Our results showed that the inner sub-shells' contribution to the overall cross section is insignificant for low impact energies; however, when increasing the impact energies, the inner shells slowly start to contribute to the overall cross section. Our CTMC results of TCS of the ionization and electron-capture channels show very good agreement with the existing theoretical and experimental data, especially in the case of electron capture at the energy range between 10 keV and 200 keV. In addition, we presented and discussed double-differential cross sections (DDCS) as function of the ionized electron energy and its ejection angle. We showed that the majority of electrons were ionized in the forward scattering, and most of the electrons were ejected with low energies, i.e., less than 12 eV. The backscattered DDCSs were generally the lowest.

Author Contributions: M.A.-A. and K.T. discussed the results and contributed to the final manuscript. M.A.-A.: analytical and numerical calculations. K.T.: development of CTMC code, performance of analytical calculations and supervised the project. All authors have read and agreed to the published version of the manuscript.

Funding: This research received no external funding.

Institutional Review Board Statement: Not applicable.

Informed Consent Statement: Not applicable.

Data Availability Statement: The data presented in this study are available in the article.

Acknowledgments: This work has been carried out within the framework of the EUROfusion Consortium, funded by the European Union via the Euratom Research and Training Programme (Grant Agreement No. 101052200—EUROfusion). Views and opinions expressed are, however, those of the author(s) only and do not necessarily reflect those of the European Union or the European Commission. Neither the European Union nor the European Commission can be held existing for them. We also acknowledge the support from the European Cost Actions CA18212 (MD-GAS).

Conflicts of Interest: The authors declare no conflicts of interest.

References

- Bandyopadhyay, I.; Barbarino, M.; Bhattacharjee, A.; Eidietis, N.; Huber, A.; Isayama, A.; Kim, J.; Konovalov, S.; Lehnen, M.; Nardon, E.; et al. Summary of the IAEA Technical Meeting on Plasma Disruptions and Their Mitigation. *Nucl. Fusion* **2021**, *61*, 077001. [\[CrossRef\]](#)
- Hollmann, E.M.; Aleynikov, P.B.; Fülöp, T.; Humphreys, D.A.; Izzo, V.A.; Lehnen, M.; Lukash, V.E.; Papp, G.; Pautasso, G.; Saint-Laurent, F.; et al. Status of Research toward the ITER Disruption Mitigation System. *Phys. Plasmas* **2015**, *22*, 021802. [\[CrossRef\]](#)
- Bakhtiari, M.; Tamai, H.; Kawano, Y.; Kramer, G.J.; Isayama, A.; Nakano, T.; Kamiya, Y.; Yoshino, R.; Miura, Y.; Kusama, Y.; et al. Study of Plasma Termination Using High- Z Noble Gas Puffing in the JT-60U Tokamak. *Nucl. Fusion* **2005**, *45*, 318–325. [\[CrossRef\]](#)
- Lehnen, M.; Alonso, A.; Arnoux, G.; Baumgarten, N.; Bozhnikov, S.A.; Brezinsek, S.; Brix, M.; Eich, T.; Gerasimov, S.N.; Huber, A.; et al. Disruption Mitigation by Massive Gas Injection in JET. *Nucl. Fusion* **2011**, *51*, 123010. [\[CrossRef\]](#)
- Manas, P.; Kappatou, A.; Angioni, C.; McDermott, R.M. ASDEX Light Impurity Transport in Tokamaks: On the Impact of Neutral Beam Fast Ions. *Nucl. Fusion* **2020**, *60*, 056005. [\[CrossRef\]](#)
- Shiraki, D.; Commaux, N.; Baylor, L.R.; Eidietis, N.W.; Hollmann, E.M.; Lasnier, C.J.; Moyer, R.A. Thermal Quench Mitigation and Current Quench Control by Injection of Mixed Species Shattered Pellets in DIII-D. *Phys. Plasmas* **2016**, *23*, 062516. [\[CrossRef\]](#)
- Whyte, D.G.; Jernigan, T.C.; Humphreys, D.A.; Hyatt, A.W.; Lasnier, C.J.; Parks, P.B.; Evans, T.E.; Taylor, P.L.; Kellman, A.G.; Gray, D.S.; et al. Disruption Mitigation with High-Pressure Noble Gas Injection. *J. Nucl. Mater.* **2003**, *313–316*, 1239–1246. [\[CrossRef\]](#)
- Morozov, D.K.; Yurchenko, E.I.; Lukash, V.E.; Baronova, E.O.; Pozdnyakov, Y.I.; Rozhansky, V.A.; Senichenkov, I.Y.; Veselova, I.Y.; Schneider, R. Mechanisms of Disruptions Caused by Noble Gas Injection into Tokamak Plasmas. *Nucl. Fusion* **2005**, *45*, 882–887. [\[CrossRef\]](#)
- Brooks, J.N. Analysis of Noble Gas Recycling at a Fusion Plasma Divertor. *Phys. Plasmas* **1996**, *3*, 2286–2292. [\[CrossRef\]](#)
- Pusztai, I.; Pokol, G.; Dunai, D.; Réfy, D.; Pór, G.; Anda, G.; Zoletnik, S.; Schweinzer, J. Deconvolution-Based Correction of Alkali Beam Emission Spectroscopy Density Profile Measurements. *Rev. Sci. Instrum.* **2009**, *80*, 083502. [\[CrossRef\]](#)
- Brix, M.; Dodt, D.; Dunai, D.; Lupelli, I.; Marsen, S.; Melson, T.F.; Meszaros, B.; Morgan, P.; Petravich, G.; Refy, D.I.; et al. Recent Improvements of the JET Lithium Beam Diagnostic. *Rev. Sci. Instrum.* **2012**, *83*, 10D533. [\[CrossRef\]](#)
- Anda, G.; Dunai, D.; Lampert, M.; Krizsanóczy, T.; Németh, J.; Bató, S.; Nam, Y.U.; Hu, G.H.; Zoletnik, S. Development of a High Current 60 keV Neutral Lithium Beam Injector for Beam Emission Spectroscopy Measurements on Fusion Experiments. *Rev. Sci. Instrum.* **2018**, *89*, 013503. [\[CrossRef\]](#)
- Réfy, D.I.; Brix, M.; Gomes, R.; Tál, B.; Zoletnik, S.; Dunai, D.; Kocsis, G.; Kálvin, S.; Szabolics, T.; JET Contributors. Sub-Millisecond Electron Density Profile Measurement at the JET Tokamak with the Fast Lithium Beam Emission Spectroscopy System. *Rev. Sci. Instrum.* **2018**, *89*, 043509. [\[CrossRef\]](#)
- Zoletnik, S.; Anda, G.; Aradi, M.; Asztalos, O.; Bató, S.; Bencze, A.; Berta, M.; Demeter, G.; Dunai, D.; Hacek, P.; et al. Advanced Neutral Alkali Beam Diagnostics for Applications in Fusion Research (Invited). *Rev. Sci. Instrum.* **2018**, *89*, 10D107. [\[CrossRef\]](#)
- Zoletnik, S.; Hu, G.H.; Tál, B.; Dunai, D.; Anda, G.; Asztalos, O.; Pokol, G.I.; Kálvin, S.; Németh, J.; Krizsanóczy, T. Ultrafast Two-Dimensional Lithium Beam Emission Spectroscopy Diagnostic on the EAST Tokamak. *Rev. Sci. Instrum.* **2018**, *89*, 063503. [\[CrossRef\]](#)
- Al Atawneh, S.J.; Tőkési, K. Target Electron Removal in $C^{5+}+H$ Collision. *Nucl. Fusion* **2022**, *62*, 026009. [\[CrossRef\]](#)
- Agueny, H.; Hansen, J.P.; Dubois, A.; Makhoute, A.; Taoutioui, A.; Sisourat, N. Electron Capture, Ionization and Excitation Cross Sections for keV Collisions between Fully Stripped Ions and Atomic Hydrogen in Ground and Excited States. *At. Data Nucl. Data Tables* **2019**, *129–130*, 101281. [\[CrossRef\]](#)

18. Ziaieian, I.; Tórkési, K. State Selective Classical Electron Capture Cross Sections in $\text{Be}^{4+} + \text{H}(1s)$ Collisions with Mimicking Quantum Effect. *Sci. Rep.* **2021**, *11*, 20164. [[CrossRef](#)]
19. Belkić, D. Electron Capture in High-Energy Ion-Atom Collisions. *Phys. Rep.* **1979**, *56*, 279–369. [[CrossRef](#)]
20. Olson, R.E. Electron Capture and Ionisation in H^+ , $\text{He}^{2+} + \text{Li}$ Collisions. *J. Phys. B At. Mol. Phys.* **1982**, *15*, L163–L167. [[CrossRef](#)]
21. Tórkési, K. State Selective Electron Capture in Low Energy Positron and Argon Collisions. *Nucl. Instrum. Methods Phys. Res. Sect. B Beam Interact. Mater. At.* **2012**, *279*, 62–65. [[CrossRef](#)]
22. Kirchner, T.; Horbatsch, M.; Keim, M.; Lüdde, H.J. State-Selective Electron-Capture Calculations for p -Ar Collisions in an Independent Many-Electron Model. *Phys. Rev. A* **2004**, *69*, 012708. [[CrossRef](#)]
23. Lin, C.D.; Tunnell, L.N. Subshell Electron Capture Cross Sections of Argon Atoms by Protons. *J. Phys. B At. Mol. Phys.* **1979**, *12*, L485–L490. [[CrossRef](#)]
24. Amaya-Tapia, A.; Martínez, H.; Hernández-Lamonedá, R.; Lin, C.D. Charge Transfer in $\text{H}^+ + \text{Ar}$ Collisions from 10 to 150 keV. *Phys. Rev. A* **2000**, *62*, 052718. [[CrossRef](#)]
25. Nikolaev, V.S. Calculation of the Effective Cross Sections for Proton Charge Exchange in Collisions with Multi-Electron Atoms. *Sov. Phys. JETP* **1967**, *24*, 163.
26. Shevelko, V.P. One-Electron Capture in Collisions of Fast Ions with Atoms. *Z. Phys. A At. Nucl.* **1978**, *287*, 19–26. [[CrossRef](#)]
27. Vinogradov, A.V.; Shevel'Ko, V.P. Role of Inner Shells in Charge-Exchange between Protons and Multielectron Atoms. *Sov. Phys. JETP* **1971**, *32*, 593–601.
28. Houamer, S.; Popov, Y.V.; Cappello, C.D. Total Cross Sections for Charge Transfer Reactions of Protons with Atomic and Molecular Targets at High Projectile Energies: The Role of Inner Orbitals. *Phys. Lett. A* **2009**, *373*, 4447–4452. [[CrossRef](#)]
29. Ciappina, M.; Barrachina, R.O.; Navarrete, F.; Olson, R.E. Classical Trajectory and Monte Carlo Techniques. In *Springer Handbook of Atomic, Molecular, and Optical Physics*; Drake, G.W.F., Ed.; Springer Handbooks; Springer International Publishing: Cham, Switzerland, 2023; pp. 919–926. ISBN 978-3-030-73892-1.
30. Garvey, R.H.; Jackman, C.H.; Green, A.E.S. Independent-Particle-Model Potentials for Atoms and Ions with $36 < Z \leq 54$ and a Modified Thomas-Fermi Atomic Energy Formula. *Phys. Rev. A* **1975**, *12*, 1144–1152. [[CrossRef](#)]
31. Green, A.E.S. An Analytic Independent Particle Model for Atoms. In *Advances in Quantum Chemistry*; Elsevier: Amsterdam, The Netherlands, 1973; Volume 7, pp. 221–262. ISBN 978-0-12-034807-7.
32. Reinhold, C.O.; Falcón, C.A. Classical Ionization and Charge-Transfer Cross Sections for $\text{H}^+ + \text{He}$ and $\text{H}^+ + \text{Li}^+$ Collisions with Consideration of Model Interactions. *Phys. Rev. A* **1986**, *33*, 3859–3866. [[CrossRef](#)]
33. Al-Ajaleen, M.S.A.; Taoutioui, A.; Tokesi, K. Charge Transfer and Ionisation Cross-Sections in Collisions of Singly Charged Lithium Ions with Helium and Nitrogen Atoms. *Plasma Phys. Control. Fusion* **2023**, *65*, 065002. [[CrossRef](#)]
34. Al-Ajaleen, M.; Tórkési, K. Total and Differential Ionization Cross Sections in Collision between Nitrogen Atom and Singly Charged Sodium Ion. *Sci. Rep.* **2023**, *13*, 14080. [[CrossRef](#)]
35. Allison, S.K. Experimental Results on Charge-Changing Collisions of Hydrogen and Helium Atoms and Ions at Kinetic Energies above 0.2 KeV. *Rev. Mod. Phys.* **1958**, *30*, 1137–1168. [[CrossRef](#)]
36. Williams, J.F.; Dunbar, D.N.F. Charge Exchange and Dissociation Cross Sections for H^{1+} , H^{2+} , and H^{3+} Ions of 2- to 50-keV Energy Incident Upon Hydrogen and the Inert Gases. *Phys. Rev.* **1966**, *149*, 62–69. [[CrossRef](#)]
37. Rudd, M.E.; DuBois, R.D.; Toburen, L.H.; Ratcliffe, C.A.; Goffe, T.V. Cross Sections for Ionization of Gases by 5-4000-keV Protons and for Electron Capture by 5-150-keV Protons. *Phys. Rev. A* **1983**, *28*, 3244–3257. [[CrossRef](#)]
38. Varghese, S.L.; Bissinger, G.; Joyce, J.M.; Laubert, R. Atomic Total Electron-Capture Cross Sections from C-, O-, F-, and S-Bearing Molecular Gases for MeV/u H^+ and He^+ Projectiles. *Phys. Rev. A* **1985**, *31*, 2202–2209. [[CrossRef](#)]
39. Almeida, D.P.; De Castro Faria, N.V.; Freire, F.L.; Montenegro, E.C.; De Pinho, A.G. Collisional Formation and Destruction of Fast Negative Hydrogen Ions in He, Ne, and Ar Targets. *Phys. Rev. A* **1987**, *36*, 16–25. [[CrossRef](#)]
40. Ormrod, J.H.; Michel, W.L. Charge Equilibrium Fractions and Charge-Exchange Cross Sections for Fast Ions in Nitrogen and Argon. *Can. J. Phys.* **1971**, *49*, 606–620. [[CrossRef](#)]
41. Morgan, T.J.; Eriksen, F.J. Single- and Double-Electron Capture by 1-100-keV Protons in Collisions with Magnesium and Barium Atoms. *Phys. Rev. A* **1979**, *19*, 1448–1456. [[CrossRef](#)]
42. Welsh, L.M.; Berkner, K.H.; Kaplan, S.N.; Pyle, R.V. Cross Sections for Electron Capture by Fast Protons in H_2 , He, N_2 , and Ar. *Phys. Rev.* **1967**, *158*, 85–92. [[CrossRef](#)]
43. Toburen, L.H.; Nakai, M.Y.; Langley, R.A. Measurement of High-Energy Charge-Transfer Cross Sections for Incident Protons and Atomic Hydrogen in Various Gases. *Phys. Rev.* **1968**, *171*, 114–122. [[CrossRef](#)]
44. Cabrera-Trujillo, R.; Amaya-Tapia, A.; Antillón, A. Differential, State-to-State, and Total-Charge-Transfer Cross Sections for H^+ Colliding with Ar. *Phys. Rev. A* **2009**, *79*, 012712. [[CrossRef](#)]
45. Afrosimov, V.; Mamaev, Y.A.; Panov, M.; Fedorenko, N. Investigation, by the Coincidence Method, of Charge State Changes Occurring in the Interaction Between H^+ , H^0 , and H^- and the Xenon Atom. *Sov. Phys. JETP* **1969**, *28*, 97–110.
46. Melo, W.S.; Santos, A.C.F.; Sant'Anna, M.M.; Sigaud, G.M.; Montenegro, E.C. Multiple Ionization of Noble Gases by 2.0 MeV Proton Impact: Comparison with Equi-Velocity Electron Impact Ionization. *J. Phys. B At. Mol. Opt. Phys.* **2002**, *35*, L187–L192. [[CrossRef](#)]
47. Cavalcanti, E.G.; Sigaud, G.M.; Montenegro, E.C.; Schmidt-B Cking, H. Absolute Cross Sections for Multiple Ionization of Noble Gases by Swift Proton Impact. *J. Phys. B At. Mol. Opt. Phys.* **2003**, *36*, 3087–3096. [[CrossRef](#)]

48. De Heer, F.J.; Schutten, J.; Moustafa, H. Ionization and Electron Capture Cross Sections for Protons Incident on Noble and Diatomic Gases between 10 and 140 keV. *Physica* **1966**, *32*, 1766–1792. [[CrossRef](#)]
49. Clementi, E.; Roetti, C. Roothaan-Hartree-Fock Atomic Wavefunctions. *At. Data Nucl. Data Tables* **1974**, *14*, 177–478. [[CrossRef](#)]
50. Bunge, C.F.; Barrientos, J.A.; Bunge, A.V. Roothaan-Hartree-Fock Ground-State Atomic Wave Functions: Slater-Type Orbital Expansions and Expectation Values for $Z = 2-54$. *At. Data Nucl. Data Tables* **1993**, *53*, 113–162. [[CrossRef](#)]
51. Khandelwal, G.S.; Choi, B.H.; Merzbacher, E. Tables for Born Approximation Calculations of K- and L-Shell Ionization by Protons and Other Charged Particles. *At. Data Nucl. Data Tables* **1969**, *1*, 103–120. [[CrossRef](#)]
52. Choi, B.-H.; Merzbacher, E.; Khandelwal, G.S. Tables for Born Approximation Calculations of L-Subshell Ionization by Simple Heavy Charged Particles. *At. Data Nucl. Data Tables* **1973**, *5*, 291–304. [[CrossRef](#)]
53. Benka, O.; Kropf, A. Tables for Plane-Wave Born-Approximation Calculations of K- and L-Shell Ionization by Protons. *At. Data Nucl. Data Tables* **1978**, *22*, 219–233. [[CrossRef](#)]
54. Johnson, D.E.; Basbas, G.; McDaniel, F.D. Nonrelativistic Plane-Wave Born-Approximation Calculations of Direct Coulomb M-Subshell Ionization by Charged Particles. *At. Data Nucl. Data Tables* **1979**, *24*, 1–11. [[CrossRef](#)]
55. Sulik, B.; Koncz, C.; Tőkési, K.; Orbán, A.; Berényi, D. Evidence for Fermi-Shuttle Ionization in Intermediate Velocity $C^+ + Xe$ Collisions. *Phys. Rev. Lett.* **2002**, *88*, 073201. [[CrossRef](#)] [[PubMed](#)]

Disclaimer/Publisher's Note: The statements, opinions and data contained in all publications are solely those of the individual author(s) and contributor(s) and not of MDPI and/or the editor(s). MDPI and/or the editor(s) disclaim responsibility for any injury to people or property resulting from any ideas, methods, instructions or products referred to in the content.